$\pi^- p$ charge-exchange analyzing power from 547 to 687 MeV/c

J. A. Wightman, A. D. Eichon,* G. J. Kim, A. Mokhtari,† and B. M. K. Nefkens
Department of Physics, University of California, Los Angeles, California 90024

W. J. Briscoe
Department of Physics, George Washington University, Washington, D.C. 20052

D. H. Fitzgerald
Los Alamos National Laboratory, Los Alamos, New Mexico 87545

M. E. Sadler
Department of Physics, Abilene Christian University, Abilene, Texas 79699
(Received 11 May 1988)

The $\pi^- p$ charge-exchange analyzing power has been measured from 547 to 687 MeV/c in the center-of-mass angular range $-0.9 \leq \cos\tilde{\theta}_\pi \leq 0.9$ using a transversely polarized target. The recoil neutron was detected in coincidence with a photon from π^0 decay. The results are compared with the three recent partial-wave analyses (PWA's); the VPI analysis is most consistent with our measured distributions except at 687 MeV/c where no PWA agrees with our data. The charge-exchange transversity cross sections are evaluated using the differential cross sections of Borcherding *et al.* These transversity cross sections are used in conjunction with earlier $\pi^\pm p$ data by our group to test the triangle inequalities which are a model-independent test of isospin invariance. Our data satisfy these inequalities everywhere; in contrast, Abaev *et al.* have reported a violation of more than 5 standard deviations at 685 MeV/c.

I. INTRODUCTION

Pion-nucleon elastic scattering ($\pi N \to \pi N$) is the simplest hadron-hadron interaction that can be determined completely. Three observables, the differential cross section $d\sigma/d\Omega$, the analyzing power A_N (or polarization P), and one of the spin-rotation parameters A or R, are needed to determine the scattering amplitudes free of ambiguities except for an overall phase. We have undertaken a program to measure the observables in $\pi^+ p \to \pi^+ p$, $\pi^- p \to \pi^- p$, and $\pi^- p \to \pi^0 n$ for incident pion momenta from 427 to 687 MeV/c. This program is unique in the sense that all reactions are measured at the same beam momenta and that all experiments are carried out by the same group at the same accelerator. The present experiment is the fourth in the series; the measurements of $d\sigma/d\Omega$ and A_N for $\pi^\pm p$ elastic scattering have already been reported.[1,2]

Accurate data on the πN system are important for testing theories of strong interactions and many quark, bag, and Skyrme-soliton models that have been advanced. Furthermore, a full set of πN data provides a model-independent test of isospin invariance at intermediate energies and momentum transfers. The πN scattering amplitudes are at the core of most descriptions of the nucleon-nucleon interaction as well as pion-nucleus scattering. We refer to our earlier papers[1,2] for a discussion of recent models; here we limit ourselves to a brief review of the πN scattering formalism and to the conventions and notations used. We compare our data to the three most recent πN partial-wave analyses, which are the common vehicle used to parametrize various πN data, and we will address aspects of isospin invariance.

II. PHENOMENOLOGY AND CONVENTIONS

A. πN scattering formalism

The amplitude for spin-0–spin-$\frac{1}{2}$ elastic scattering, constrained by parity and rotational invariance, is given by

$$M = f - ig\boldsymbol{\sigma}\cdot\hat{\mathbf{n}}, \quad \hat{\mathbf{n}} = \frac{\hat{\mathbf{k}}_i \times \hat{\mathbf{k}}_f}{|\hat{\mathbf{k}}_i \times \hat{\mathbf{k}}_f|} ,$$

where f is the spin-nonflip amplitude, g is the spin-flip amplitude, the σ's are the Pauli spin operators, $\hat{\mathbf{n}}$ is a unit vector normal to the scattering plane, and the phase convention of Williams[3] has been used. The differential cross section is given by

$$d\sigma = d\sigma_{\text{unpol}}[1 + A_N(\theta)\mathbf{P}_t\cdot\hat{\mathbf{n}}] ,$$

where $\mathbf{P}_t$ is the polarization of the target nucleon. The unpolarized differential cross section is

$$d\sigma_{\text{unpol}} = |f|^2 + |g|^2$$

and the analyzing power A_N is given by

$$A_N(\theta) = \frac{2\,\text{Im}(f^* g)}{|f|^2 + |g|^2} .$$

It follows that

$$d\sigma_\uparrow = d\sigma_{\text{unpol}}[1 + A_N(\theta)] = |f - ig|^2$$

and

$$d\sigma_{\downarrow}=d\sigma_{\text{unpol}}[1-A_N(\theta)]=|f+ig|^2 ,$$

where $\mathbf{P}_t$ and $\hat{\mathbf{n}}$ are parallel ($\uparrow$) or antiparallel ($\downarrow$). These cross sections are known as the transversity cross sections and are determined, in practice, by combining the unpolarized cross sections with the analyzing power data. The analyzing power is determined experimentally using the relation

$$A_N=\frac{1}{P_t}\frac{(d\sigma)_L-(d\sigma)_R}{(d\sigma)_L+(d\sigma)_R} ,$$

where L (R) refers to pion scattering to beam left (right).

B. Isospin

When the interaction Hamiltonian is invariant under isospin I, only two scattering amplitudes are needed, F_1 and F_3 for $I=\frac{1}{2}$ and $I=\frac{3}{2}$, respectively. The isospin decomposition of the scattering amplitudes is

$$F^+\equiv F(\pi^+p\to\pi^+p)=F_3 ,$$

$$F^-\equiv F(\pi^-p\to\pi^-p)=\tfrac{1}{3}F_3+\tfrac{2}{3}F_1 ,$$

$$F^0\equiv F(\pi^-p\to\pi^0n)=\frac{\sqrt{2}}{3}(F_3-F_1) .$$

These amplitudes form a triangle in the complex plane

$$F^+=(F^-+\sqrt{2}F^0) .$$

The triangle inequalities for the transversity cross sections are

$$\tfrac{1}{2}(\sqrt{d\sigma_{\uparrow}^+}-\sqrt{d\sigma_{\uparrow}^-})^2\le d\sigma_{\uparrow}^0\le\tfrac{1}{2}(\sqrt{d\sigma_{\uparrow}^+}+\sqrt{d\sigma_{\uparrow}^-})^2 \tag{1a}$$

and

$$\tfrac{1}{2}(\sqrt{d\sigma_{\downarrow}^+}-\sqrt{d\sigma_{\downarrow}^-})^2\le d\sigma_{\downarrow}^0\le\tfrac{1}{2}(\sqrt{d\sigma_{\downarrow}^+}+\sqrt{d\sigma_{\downarrow}^-})^2 . \tag{1b}$$

A 5σ violation of the triangle inequalities in four consecutive data points has been reported for the transversity-down cross sections at $p_\pi=685$ MeV/c near $\cos\theta=-0.8$ by the Leningrad group.[4] The input data came from three different groups working at slightly different beam momenta. The charge-exchange (CEX) A_N data were measured by the Rutherford group[5] and were the only CEX A_N data available at that time. Alder and co-workers[6] did not see a violation of the triangle inequalities at $p_\pi=351$, 408, and 427 MeV/c. Their energy-independent partial-wave analysis indicated a small isospin violation: namely, a difference of $(2.0\pm0.4)^\circ$ in the phase of the P_{33} wave measured in π^+p and π^-p scattering at $p_\pi=408$ MeV/c.

For unpolarized data, the two sets of inequalities in Eq. (1) reduce to a single set

$$\tfrac{1}{2}(\sqrt{d\sigma^+}-\sqrt{d\sigma^-})^2\le d\sigma^0\le\tfrac{1}{2}(\sqrt{d\sigma^+}+\sqrt{d\sigma^-})^2 .$$

Comiso *et al.*[7] tested isospin invariance with this relation over the range $p_\pi=239$–371 MeV/c and found the inequality satisfied.

Many models of the strong interaction allow for a small violation of isospin invariance. For instance, when meson exchange is involved, one can have isospin breaking by isovector-isoscalar meson mixing,[8] primarily ρ-ω and π^0-η. A good energy region in which the π^0-η mixing may manifest itself is near the η-production threshold, which is just accessible at LAMPF and covered in this experiment. Cutkosky[9] investigated π^0-η mixing via the $S_{11}(1535)$ and predicted possible isospin-violating effects up to 20% in the backward direction. In the quark model the violation of isospin invariance is a consequence of the mass difference between the u and d quark, which is non-Coulombic in origin. Estimates of this difference are generally 3–5 MeV which, compared to a constituent mass of a few hundred MeV, leads one to expect that the violation will be small.

C. Partial-wave analyses

The most recent partial-wave analysis was made by the Virginia Polytechnic Institute and State University (VPI) group.[10] The two other major, but older, analyses are by the Karlsruhe-Helsinki (K-H) group[11] (1980) and the Carnegie-Mellon University–Lawrence Berkeley Laboratory (C-L) Collaboration.[12] The VPI group only reports the resonances in terms of their pole positions in the complex energy plane. Interestingly, they show two P_{11} poles: $P_{11}(\text{I})=(1359-100i)$ MeV and $P_{11}(\text{II})=(1410-80i)$ MeV. Ayed and Bareyre[13] had earlier proposed two nearby P_{11} resonances with masses of 1413 and 1532 MeV based on the Saclay partial-wave analysis. However, such a split in the P_{11} is not seen in the K-H or C-L analyses.

III. EXPERIMENT

The experiment was performed at the Clinton P. Anderson Meson Physics Facility (LAMPF) using the P^3 channel. The central momentum, momentum bite, and flux of each pion beam are given in Table I. The momenta are the same as those of the differential-cross-section measurements for $\pi^\pm p$ elastic scattering[1] and CEX (Ref. 14) and the analyzing powers for elastic scattering.[2] The central beam momentum of the P^3 channel is known to $\pm0.3\%$ from time-of-flight[15] and range measurements.[16] The experimental setup is shown in Fig. 1; details are given in Ref. 17. After exiting the channel, the beam

TABLE I. π^- beam characteristics.

p (MeV/c)	$\Delta p/p$ (% FWHM)	$\sqrt{s}$ (MeV)	Rate (10^6 π/sec)
547	1.3	1400	1.1
586	2.4	1425	1.1
625	1.6	1450	0.8
657	4.0	1470	1.0
687	5.3	1488	0.6

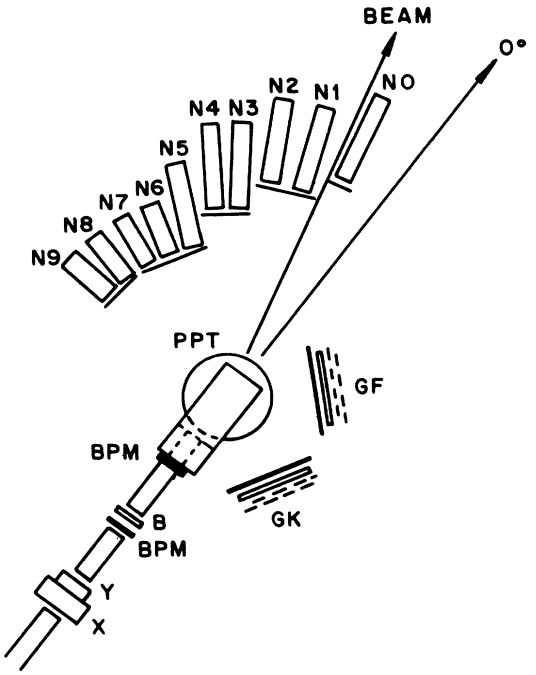

FIG. 1. The experimental setup.

passed through a horizontal (X) and a vertical (Y) steering magnet. The horizontal steering was necessary to compensate for the bending of the incident beam in the field of the polarized-target magnet. A 2 cm$\times$2 cm beam spot was measured using Polaroid film placed against the target cryostat. The position of the beam was monitored continuously by two beam-profile monitors (BPM's), and the beam flux was measured by two counter telescopes placed in the beam halo above and below the beam along with a small counter hodoscope (B) placed directly in the beam.

The polarized proton target (PPT) from LANL group P-7 has been detailed in Ref. 18. The target cell was located between the poles of a large C-shaped magnet which produced a field of 25 kG uniform to ± 3 G over the volume of the cell. The beam passed through a hole in the magnet yoke before impinging on the target cell; this arrangement increased the angular acceptance of the detectors. The cell containing the propanediol target material was a cylinder 2 cm in diameter and 4 cm long oriented with the axis along the beam direction. The free protons in the target were dynamically polarized transverse to the scattering plane. The target polarization was typically 82% with an overall systematic uncertainty of $\pm 3\%$ based on the uncertainty in the calibration.

Recoil neutrons were detected in ten pairs of scintillation counters covering the range $-0.9 \leq \cos\tilde{\theta}_\pi \leq 0.9$. Two neutron counters at a given angle were stacked vertically, and they were centered about the horizontal scattering plane. We found that pairing the neutron counters was a good way to monitor possible drifts in the efficiency. The counters were cylinders 7.6 cm in diameter. The lengths (45.7 cm for $N0$–$N5$ and 19.1 cm for $N6$–$N9$) were chosen to give a high detection efficiency (25–35%) without compromising the timing resolution (1.5–5 ns). To have sufficient temporal separation between the prompt events and the CEX neutrons, the flight paths were of different lengths, ranging from 2.5 m for $N9$ (slowest) to 4 m for $N0$ (fastest). The discriminator thresholds were set at 50 mV, except for $N0$ and $N1$ which were set at 100 mV due to their proximity to the beam. The 50 mV corresponds to a neutron threshold of 2–3 MeV. The gain of each photomultiplier tube (PMT) was set using the Compton edge of ^{60}Co and was monitored periodically throughout the experiment to correct any drifts. These counters were the same ones used in the CEX differential cross-section measurements of Ref. 14. Thin scintillation counters were placed in front of the neutron detectors to veto charged-particle events.

Photons from the $\pi^0 \rightarrow 2\gamma$ decay registered in the photon detectors GF and GK; only one of the photons was required in the event trigger. The spatial distribution of single photons from π^0 decay is maximum along the direction of flight of the π^0. This allowed us to "match" kinematically GF with $N5$–$N9$ and GK with $N0$–$N4$. Each photon detector consisted of a lead converter sheet 9.5 mm thick (1.7 radiation lengths), a multiwire proportional chamber (MWPC) measuring 100 cm$\times$60 cm and a triggering hodoscope comprised of eight overlapping, scintillation counters. Each of the hodoscope counters had a photomultiplier tube on either end of it. Eight thin, overlapping scintillation counters in front of the lead converter were used to veto charged-particle events. These photon detectors had been used previously as well.[14] The triggering counters provided the signal for a photon and the timing of the master event trigger. A photon trigger consisted of a signal in at least one hodoscope counter and no signal in the veto counters. The MWPC information was used for qualitative investigations only because of some variation in the efficiency of the chambers between the time of the data runs and the background runs with the dummy target, and it did not form part of the hardware trigger.

CEX candidate events required a coincidence between a beam particle, a neutron, a photon trigger, and no dead-time signal. The dead time was 2–3% throughout the experiment. For each event, pulse heights and timing signals were recorded for each neutron counter, beam hodoscope counter, and each photomultiplier tube of the photon trigger counters. Finally, the position of each photon shower in the MWPC's was also recorded.

IV. DATA ANALYSIS

The analyzing power is calculated from the expression

$$A_N = \frac{1}{P_t} \frac{N_\downarrow - N_\uparrow}{N_\downarrow + N_\uparrow - 2B} , \tag{2}$$

where P_t is the target polarization, $N_\downarrow$ ($N_\uparrow$) is the normalized yield for target spin down (up), and B is the normalized yield from the background target. The yield of CEX events was obtained from the neutron time-of-flight (TOF) spectra, a typical example of which is shown in Fig. 2.

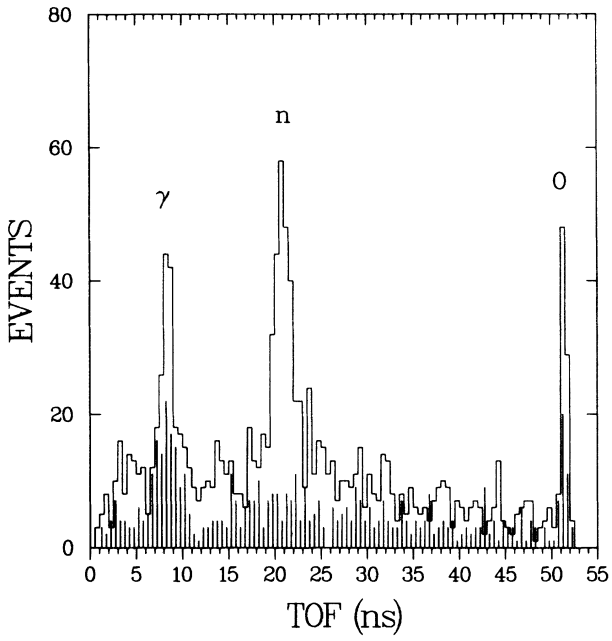

FIG. 2. Typical neutron TOF spectrum in counter $N7$ ($p_\pi = 625$ MeV/c, $T_n = 95.5$ MeV). γ are the prompt events, n the neutrons, and 0 the overflows. The TOF start is given by the photon signal. The bar plot is the background from a carbon-target run.

A. Data cuts in the off-line analysis

The off-line analysis was made in several passes, adding additional constraints or cuts to each pass. The analyzing power and its uncertainty were calculated after each pass; the successive passes were found to be mutually consistent within the uncertainties. There were no cuts in the first pass as it served as the baseline. In the second pass, we examined the effect of a good MWPC hit defined as a coincidence between the two planes of wires (x and y) in the chamber. We found the chamber efficiency to be somewhat erratic, and we decided to omit this requirement for the remainder of the analysis.

In the third pass, cuts were applied on the photon spatial distribution in the hodoscope and on the neutron and photon multiplicities. This cut, based on the peaking of the angular distribution of single photons from π^0 decay along the π^0 direction, defined an angular region about the π^0 direction which was typically $19° \times 28°$ for GF and $24° \times 38°$ for GK. The vertical cut was made possible using the timing difference between the two ends of the photon hodoscope counters. The horizontal cut was made by selecting only four or five counters for a given π^0 angle. This reduced the background by a factor of 2–3 with little loss of CEX signal. This cut was also used to remove the radiative-capture, $\pi^- p \to \gamma n$, events. The kinematic shadow of the neutron counter on the photon detector for the radiative capture events was typically $3° \times 4°$ for GF and $4° \times 4°$ for GK; exclusion of the shadow region removes these events with only a small loss of CEX events. The multiplicity cuts required a single neutron-counter hit and one or two photons in each event. Of the total number of events, 94% contained only a single neutron-counter hit with the remaining 6% predominantly double neutron hits. The double-neutron events came from two sources: cross scattering between the two counters of a given pair ($\sim 4\%$) and two counters from different positions firing ($\sim 2\%$), which is a measure of the random-event rate. The geometry of the photon detectors was such that with the spatial distribution cut, only single photons would be seen in either detector. Because of the overlap of the hodoscope counters, it is possible to have two photon signals so that up to two photons were permitted in each event. Only about 3% of the total events contained more than two photons.

The fourth and final pass in the analysis added cuts on the neutron pulse height and beam TOF. These cuts improved the signal-to-background ratio by $\sim 50\%$ for the higher-energy neutrons. In the final analysis, the signal-to-background ratio varied monotonically from about 3:1 to about 1:4 as the neutron energy increased (from counter $N9$ to $N0$). The signal-to-background ratio is not as important as carefully monitoring the normalization because Eq. (2) is a ratio of numbers of events.

B. Sources of background

Only 7% of the target by weight was hydrogen; the rest was mainly carbon and oxygen. Furthermore, there were the target housing and cryostat along with the cryogenic liquids, ^{3}He and ^{4}He. The shape of the background event distribution was measured with the propanediol replaced by graphite beads of approximately the same density. We assumed that the quasielastic charge-exchange scattering by carbon is similar to that by the other complex nuclei in the target. For the background studies, the carbon beads were placed in the target cylinder inside the cryostat with the target running at its normal operating temperature; only the microwaves were turned off. We expected the background to be polarization independent which we did verify by subtracting the spin-down yield from the spin-up yield and finding that nothing remains outside of the peak region, see Fig. 3(a).

C. Beam normalization

It follows from Eq. (2) that only a relative normalization was needed for evaluating the spin-up and spin-down scattering yields. All runs were normalized with respect to the spin-up runs. The beam normalization was determined in three ways using the yields of (a) the off-time events (those events in the neutron TOF spectra at times later than the CEX neutrons, see Fig. 2), (b) the prompt events, and (c) the beam monitors. The normalization based on off-time events obviates the need for correction factors due to beam wander, changes in the gain of the PMT's, and efficiency of the MWPC's. However, this normalization suffers from low statistics, especially for the final set of cuts. For each beam momentum and cart position, we computed the normalization factor as the weighted average of the normalization factors for each individual counter. The individual normalization factors were compared with the average, and any that were more than 2.5 standard deviations from the average were re-

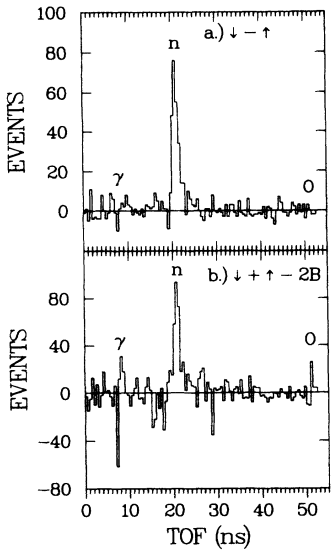

FIG. 3. Sum and difference TOF spectra for counter $N7$ ($p_\pi = 625$ MeV/c). (a) Events $= \downarrow - \uparrow$, the net number of events in the range 25 to 48 nsec is $+5 \pm 24$ and (b) events $= \downarrow + \uparrow - 2B$, the net events from 25 to 48 nsec are $+27 \pm 33$.

moved from the average, which was recomputed. For the total data sample, this resulted in about 2% of the counters being removed from the average for $\uparrow/\downarrow$ and about 7% for $\uparrow/B$.

The second method was to calculate the normalization from the number of events in the prompt-event peak, labeled γ in Fig. 2. These events are predominantly due to low-energy photons from nuclear deexcitation in the target and cryostat. The normalization factors calculated from these events were of the same statistical precision (1–4 % depending on the set of cuts) for each momentum and cart position as those from the off-time events. The weighted-average normalization was calculated as above, and resulted in the removal of about 5% of the counters from the average for $\uparrow/\downarrow$ and about 4% for $\uparrow/B$, again for the total data sample. The weighted average of the prompt-event normalization with the off-time normalization was computed to yield the "histogram" normalization. We used the "histogram" normalization factors for the normalization except at 687 MeV/c.

The third determination of the normalization factor was based on the number of events in the beam counter and is referred to as the scaler normalization. Since the scaled events in the beam counter were 10^{10}–10^{11} for each run, the statistical uncertainty is $\ll 1\%$ and is not included in Table II. Because the signal runs were taken with alternating polarization direction, we required that the scaler normalization for $\uparrow/\downarrow$ be consistent with the "histogram" normalization. This was not the case for the background normalization as the background runs were taken after all the signal runs had been completed and required retuning the beam. The normalization factors for $\uparrow/\downarrow$ and $\uparrow/B$ at each cart position are compared in Table II. The data at 687 Mev/c were taken in two sets of data runs between which some of the trigger electronics were changed. This change involved replacing the constant-fraction discriminators. At the same time, the duty factor of the accelerator was increased from 6% to 9%. The combination of these two effects resulted in enough difference between the two sets to require that they be handled separately. This only affects the 687-MeV/c data as all other data were taken after these changes were made. With the background runs at 687 MeV/c taken after the electronics change, we found that only the scaler normalization produced a consistent set of results for the two cart positions and both sets of runs.

A further check on the normalization was performed by forming the combinations $\downarrow - \uparrow$ and $\downarrow + \uparrow - 2B$ in Fig. 3. In both cases, only the CEX neutron peak remains. The regions outside of the peak are flat, and the net number of events there is consistent with zero.

D. Uncertainties

The uncertainties are divided into three categories: statistical, systematic, and normalization. The statistical uncertainty in A_N is given by

$$\sigma_{A_N} = 2P_t \left[\frac{A_N}{N_\downarrow - N_\uparrow} \right]^2 [(N_\uparrow - B)^2 \sigma_\downarrow^2 + (N_\downarrow - B)^2 \sigma_\uparrow^2 + (N_\downarrow - N_\uparrow)^2 \sigma_B^2]^{1/2} ,$$

TABLE II. Comparison of the normalization factors at each momentum for the forward and backward cart positions. The "histogram" normalization factor is the weighted average of the off-time and prompt-event normalization factors and the scalar normalization factor is calculated from the beam monitor which has a statistical uncertainty $\ll 1\%$. For the background normalization ($\uparrow/B$), the agreement between histogram and scaler factors is not required, as explained in Sec. IV C.

p_π (MeV/c)	Normalization factor	Forward $\uparrow/\downarrow$	Forward $\delta\uparrow/\downarrow$	Backward $\uparrow/\downarrow$	Backward $\delta\uparrow/\downarrow$	Forward $\uparrow/B$	Forward $\delta\uparrow/B$	Backward $\uparrow/B$	Backward $\delta\uparrow/B$
547	Histogram	0.72	0.01	1.07	0.01	0.57	0.01	1.20	0.02
	Scaler	0.74		1.08		0.57		0.95	
586	Histogram	0.98	0.01			1.18	0.01		
	Scaler	1.01				1.08			
625	Histogram	0.99	0.02	1.38	0.02	1.95	0.04	1.15	0.01
	Scaler	1.02		1.39		1.79		1.10	
657	Histogram	0.98	0.01			1.26	0.02		
	Scaler	1.01				1.35			
687	Histogram	0.92	0.02	1.04	0.04	1.40	0.05	1.40	0.06
	Scaler	0.95		1.08		1.30		1.41	

where

$$\sigma_{\uparrow}^2 = N_{\uparrow}, \quad \sigma_{\downarrow}^2 = \eta_{\downarrow} N_{\downarrow}, \quad \sigma_B^2 = \eta_B B ,$$

and $\eta_{\downarrow}$ and η_B are the $\uparrow/\downarrow$ and $\uparrow/B$ normalization factors, respectively.

The systematic uncertainty is due to the uncertainty in the target polarization and is estimated to be $\pm 3\%$. This is based on an analysis of the sources of uncertainty in determining the polarization including the consistency of the calibration. The NMR signal is calibrated using the natural polarization of the free protons at 1 K; this procedure is detailed in Ref. 18. Four sets of thermal-equilibrium calibration runs were taken during the experiment; they are consistent to 1%. Sources of uncertainty in determining the polarization are the following. The enhanced polarization NMR signal is 2–3 orders of magnitude larger than the calibration signal, and the amplifier is not perfectly linear over such a large range. The NMR signal is measured by a diode whose response is also not perfectly linear. The calibration is contingent upon knowing the temperature of the target; this requires measuring the ^{3}He vapor pressure and relies on the calibration of the pressure gauge. These considerations form the basis for our estimate of $\pm 3\%$ for the systematic uncertainty. Because of its effect upon the analyzing powers, the systematic uncertainty has been handled separately from the statistical uncertainty. The target polarization appears as a multiplicative factor in Eq. (2), and the uncertainty in it scales the analyzing powers.

The uncertainty in $\eta_{\downarrow}$ is $\pm 1\%$, based on an analysis of the relative beam monitors, see Table II. For all data except at 687 MeV/c, the uncertainty in η_B is $\pm 5\%$. There are a number of contributors to this uncertainty besides the statistical uncertainty and the consistency among the normalization factors. The background target measurements were taken some time after the data taking was completed, and they required retuning of the beam and adjustment of the neutron counters. Also, the ratio of the densities of the propanediol target to the background target could not be established by weighing as that would have required melting the target material which was needed for a subsequent experiment. The 687-MeV/c data were taken in two sets of runs separated in time and involving a change in the trigger electronics. We estimate an error of $\pm 10\%$ in η_B for these data. The uncertainty in η_B has been included in the error in A_N by

$$\delta A_N = [(A_N - A_N')^2 + \sigma_{A_N}^2]^{1/2} , \tag{3}$$

where A_N and σ_{A_N} are calculated using the nominal values for the normalization and A_N' is the analyzing power with η_B increased (or decreased) by its uncertainty.

V. RESULTS AND DISCUSSION

The results of the analyzing-power measurements are tabulated in Table III and shown in Fig. 4. The quoted errors are the statistical and beam normalization errors combined in quadrature as given by Eq. (3). The systematic uncertainty of $\pm 3\%$ due to the target-polarization calibration error is not included.

The comparison of A_N(CEX) with $A_N(\pi^{\pm} p \to \pi^{\pm} p)$ *vis-à-vis* the different PWA's at 625 MeV/c is illustrated in Fig. 5. The charge-exchange channel shows greater differences between the PWA's than the elastic channels. Thus, $A_N(\pi^- p \to \pi^0 n)$ appears to be the most sensitive means of distinguishing the PWA's.

The numerical comparison of the present experiment with the three recent PWA's is made in Table IV using the quantity

$$\chi^2 = \frac{1}{n} \sum \frac{(A_N - A_N^{\mathrm{PWA}})^2}{\delta_A^2} ,$$

where n is the number of data points. The VPI PWA results used in this comparison are from the fall 1984 analysis and do not include the present measurements. The effect of the 3% systematic uncertainty from the target polarization is always small and has not been included. At the lower momenta, the VPI solution is preferred but not overwhelmingly. We previously reported[17] a ninth point at 586 MeV/c ($\cos\theta = -0.94$). This point is somewhat suspect due to lack of consistency between the two counters of the pair, and we have omitted it here. Our group has recently obtained some high-precision data on $A_N(\pi^- p \to \pi^0 n)$ in the backward direction[19] at some selected angles which very clearly support the VPI PWA. At the higher momenta, the data show no clear choice among the PWA's, while at 687 MeV/c, none of the PWA predictions is consistent with our measured distribution.

The present measurements along with those of Refs. 2 and 19 were added to the VPI data base prior to the summer 1986 analysis. The largest changes in the phases from the fall 1984 analysis which contains none of these measurements are $-2.21°$ for the P_{11}, $-1.17°$ for the P_{31}, and $+1.84°$ for the S_{11}, all at 687 MeV/c.

Our results are compared with the Rutherford[5] A_N data at the incident energies nearest to ours in Fig. 6; the agreement with our data is not satisfactory. Earlier, the Karlsruhe group had questioned the validity of the data of Ref. 5 (Ref. 11). We have investigated improving the consistency of the two data sets by lowering the Rutherford beam momenta by 5–8 % as shown in Fig. 7. The agreement is acceptable, except again with our 687-MeV/c data. All of the distributions have a similar shape for $\cos\theta > 0$, and the relatively large error bars on the Rutherford data for $\cos\theta < 0$ weaken any comparison. In fact, our 586-MeV/c data are consistent with all of the Rutherford distributions up to and including 723 MeV/c. There is a peculiar spike around $\cos\theta = -0.8$ in the Rutherford 675-MeV/c data which is not observed in this experiment at either 657 or 687 MeV/c. The absence of this spike is important because it appears that the spike is the origin of the violation of isospin invariance reported by the Leningrad group.[4] There is also a spike in the Rutherford 698-MeV/c data around $\cos\theta = -0.6$ which does not coincide with the angular interval of the violation.

We combine our earlier results for the differential cross sections, $d\sigma^{\pm}$ (Ref. 1) and $d\sigma^0$ (Ref. 14), and analyzing powers $A_N^{\pm}$ (Ref. 2) with our present results for A_N^0 at the

TABLE III. The charge-exchange analyzing power. The uncertainty is given by Eq. (5). The cosθ interval is given by the size of the counters and target.

p_π (MeV/c)	cos$\tilde{\theta}_\pi$	A_N	δ_A	p_π (MeV/c)	cos$\tilde{\theta}_\pi$	A_N	δ_A
547	−0.62±0.05	−0.08	0.21	586	−0.59±0.05	0.06	0.23
	−0.43±0.05	−0.19	0.31		−0.39±0.05	0.14	0.13
	−0.22±0.05	0.33	0.09		−0.18±0.05	0.39	0.14
	−0.01±0.05	0.81	0.20		0.03±0.05	0.71	0.14
	0.18±0.05	1.06	0.14		0.22±0.05	0.95	0.12
	0.38±0.05	1.15	0.13		0.41±0.05	0.96	0.12
	0.58±0.05	0.81	0.07		0.61±0.05	0.69	0.06
	0.79±0.04	0.43	0.03		0.81±0.04	0.43	0.04
625	−0.93±0.02	0.42	0.25	657	−0.94±0.02	0.09	0.13
	−0.76±0.04	0.48	0.32		−0.75±0.04	−0.02	0.27
	−0.55±0.04	0.68	0.29		−0.53±0.04	−0.01	0.13
	−0.35±0.05	0.33	0.14		−0.32±0.04	0.21	0.29
	−0.14±0.05	0.50	0.13		−0.11±0.04	0.34	0.15
	0.07±0.05	0.80	0.13		0.10±0.04	0.51	0.15
	0.26±0.05	1.13	0.18		0.28±0.04	0.94	0.18
	0.45±0.04	1.04	0.10		0.47±0.04	0.89	0.12
	0.64±0.04	0.77	0.06		0.66±0.04	0.69	0.07
	0.83±0.03	0.45	0.05		0.84±0.03	0.46	0.05
687	−0.93±0.02	−0.07	0.11				
	−0.73±0.04	−0.16	0.20				
	−0.51±0.04	−0.12	0.11				
	−0.30±0.04	−0.01	0.14				
	−0.09±0.04	−0.06	0.14				
	0.13±0.04	0.32	0.08				
	0.31±0.04	0.73	0.13				
	0.49±0.04	0.70	0.08				
	0.68±0.03	0.63	0.06				
	0.86±0.03	0.40	0.12				

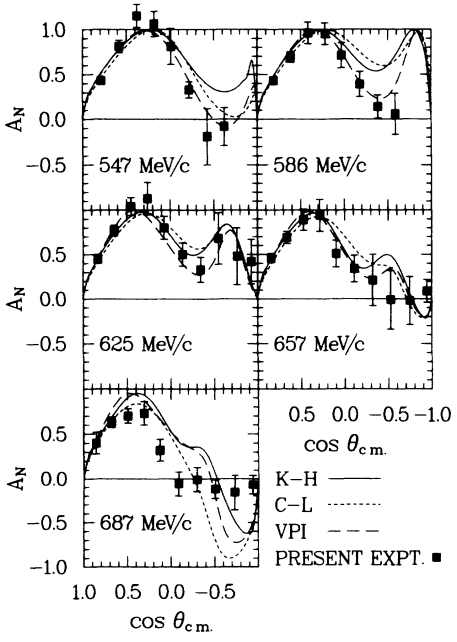

FIG. 4. The present charge-exchange analyzing powers and the predictions of the three recent PWA's: K-H (Ref. 11), C-L (Ref. 12), and VPI (Ref. 10).

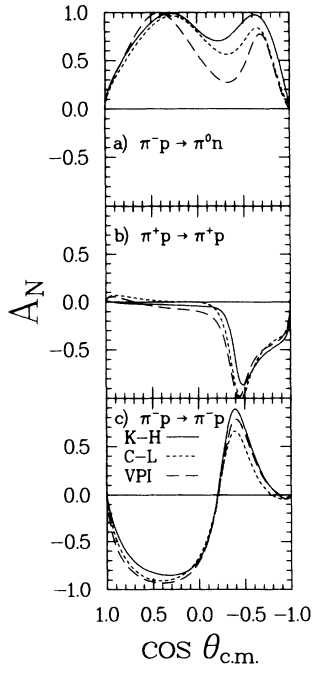

FIG. 5. Comparison of the analyzing powers in the charge-exchange and $\pi^\pm p$ elastic-scattering channels. The curves are the recent PWA's.

TABLE IV. χ^2 consistency test of the measured distributions with Ref. 10 (VPI), Ref. 11 (K-H), and Ref. 12 (C-L); ν is the number of degrees of freedom.

p_π (MeV/c)	VPI	K-H	C-L	ν
547	11.3	28.7	17.6	8
586	6.1	24.1	29.0	8
625	5.6	5.6	11.7	10
657	13.3	9.9	14.6	10
687	65.4	64.5	75.9	10

same momenta to obtain the transversity cross sections and to test isospin invariance in the πN system using the triangle inequalities. A fit to the data is necessary to obtain the bounds since $d\sigma$ and A_N have been measured at different scattering angles. The procedure is detailed in Ref. 2 and summarized as follows.

(a) The differential cross sections are fit to Legendre polynomials using a least-squares routine.

(b) The polynomials are evaluated at angles where we have measured the analyzing powers to calculate $d\sigma_\uparrow$ and $d\sigma_\downarrow$ with their errors.

(c) New Legendre polynomials are fit to $d\sigma_\uparrow$ and $d\sigma_\downarrow$.

(d) These new Legendre polynomials are used to calculate the bounds of the triangle inequalities for the transversity cross sections and their uncertainties.

The transversity-up and -down cross sections were fit

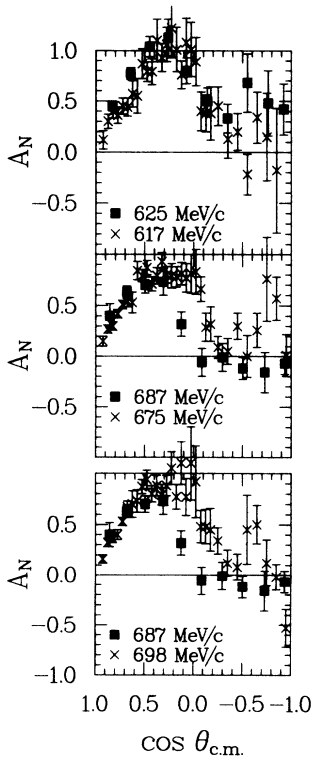

FIG. 6. Comparison of the present measurements (squares) with those of Ref. 5 ($\times$'s).

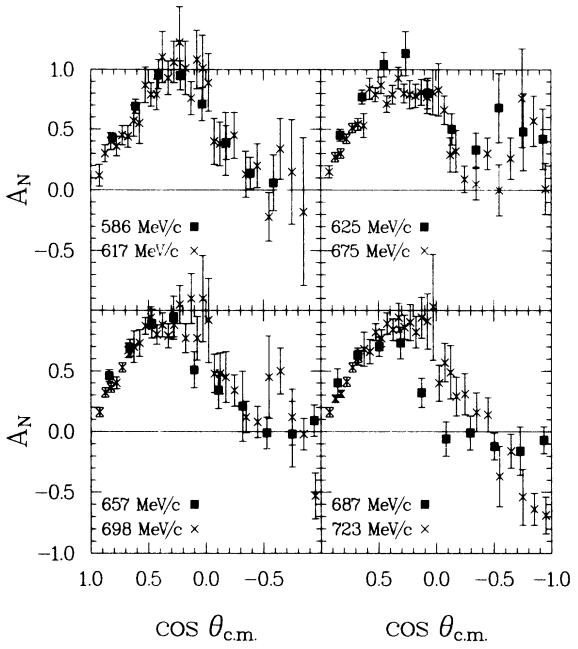

FIG. 7. Comparison of the present measurements (squares) with those of Ref. 5 ($\times$'s) where the beam energy of Ref. 5 is reduced by $\sim 5\%$.

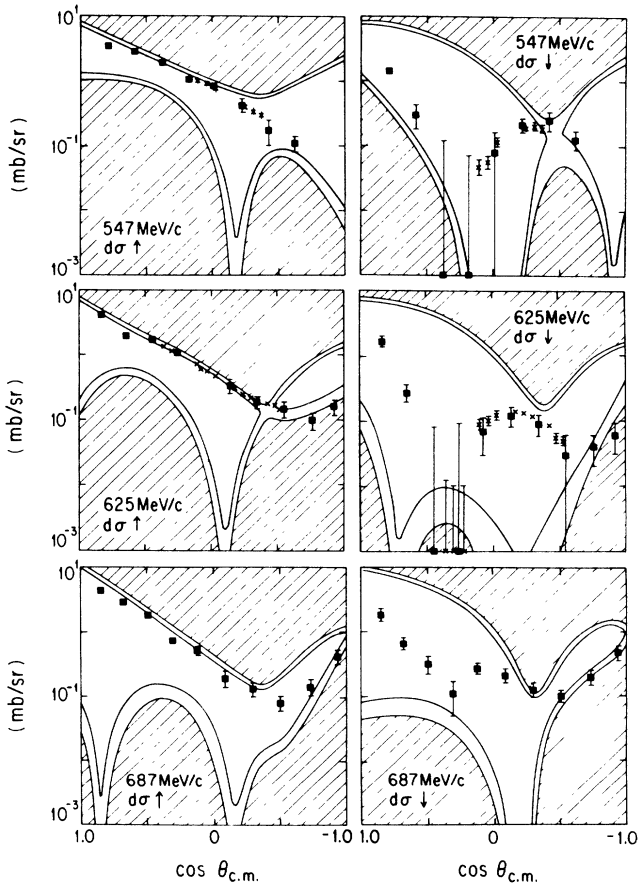

FIG. 8. The triangle inequalities for the transversity-up ($d\sigma_\downarrow$) and transversity-down ($d\sigma_\downarrow$) cross sections as a model-independent test of isospin invariance in the πN system up to the η-production threshold. The shaded region is disallowed by isospin invariance. The $\times$'s are from Ref. 19.

TABLE V. The center-of-mass transversity cross sections. The limits on $\cos\theta$ are given by the size of the counters and target.

p_π (MeV/c)	$\cos\tilde{\theta}_\pi$	$d\sigma_\uparrow$ (mb/sr)	$d\sigma_\downarrow$ (mb/sr)
547	−0.62±0.05	0.11±0.03	0.13±0.04
	−0.43±0.05	0.17±0.07	0.25±0.08
	−0.22±0.05	0.41±0.09	0.21±0.05
	−0.01±0.05	0.78±0.11	0.08±0.09
	0.18±0.05	1.03±0.12	0±0.07
	0.38±0.05	2.00±0.23	0±0.12
	0.58±0.05	2.86±0.29	0.30±0.11
	0.79±0.04	3.53±0.35	1.41±0.16
625	−0.93±0.02	0.16±0.04	0.06±0.03
	−0.76±0.04	0.10±0.03	0.04±0.02
	−0.55±0.04	0.15±0.04	0.03±0.03
	−0.35±0.05	0.19±0.04	0.09±0.03
	−0.14±0.05	0.34±0.08	0.12±0.04
	0.07±0.05	0.61±0.07	0.07±0.04
	0.26±0.05	1.09±0.14	0±0.09
	0.45±0.04	1.73±0.18	0±0.08
	0.64±0.04	2.01±0.21	0.27±0.08
	0.83±0.03	4.31±0.45	1.65±0.21
687	−0.93±0.02	0.41±0.10	0.47±0.11
	−0.73±0.04	0.14±0.04	0.20±0.05
	−0.51±0.04	0.08±0.02	0.10±0.02
	−0.30±0.04	0.13±0.03	0.13±0.03
	−0.09±0.04	0.19±0.05	0.21±0.05
	0.13±0.04	0.51±0.07	0.27±0.05
	0.31±0.04	0.73±0.09	0.11±0.06
	0.49±0.04	1.84±0.21	0.32±0.09
	0.68±0.03	2.90±0.31	0.66±0.13
	0.86±0.03	4.31±0.57	1.85±0.41

simultaneously using least squares such that $d\sigma_\uparrow + d\sigma_\downarrow = 2\,d\sigma$. Since $A_N = 0$ at 0° and 180°, constraints were added to the fitting procedure which forced $d\sigma_\uparrow = d\sigma_\downarrow = d\sigma$ at these angles. Another constraint was added to prevent the fit for $d\sigma_\uparrow$ and $d\sigma_\downarrow$ from assuming values which would require $|A_N| \geq 1$.

The results of our test of isospin invariance at 547, 625, and 687 MeV/c are shown in Fig. 8. The data of Ref. 14 have been corrected where necessary for radiative capture contamination using the compilation of Ref. 20. The CEX transversity cross sections are compiled in Table V. There is no evidence for a violation of isospin invariance. The violation of isospin invariance reported by the Leningrad group[4] for transversity-down data at 685 MeV/c is not substantiated by any of our data. We have not included the Rutherford[5] data at 675 MeV/c in Fig. 8 because they are at a lower momentum than our 687 MeV/c data, lying at the lower limit of our momentum bite. The three transversity-up plots in Fig. 8 share an interesting feature, namely the CEX data closely follow the upper bound in the forward hemisphere and cross over to follow the lower bound at far backward angles.

VI. SUMMARY AND CONCLUSIONS

We have measured angular distributions of the analyzing power in $\pi^- p \to \pi^0 n$ from 547 to 687 MeV/c. Our data at 547, 586, and 625 MeV/c favor the VPI PWA over the ones by K-H and C-L. The 657-MeV/c data show no clear preference among the PWA's, while none of them are consistent with our distribution at 687 MeV/c. Our data combined with cross-section measurements yield transversity-up and -down cross sections that fall within the limits of the triangle inequalities derived from $\pi^\pm p \to \pi^\pm p$ data. Therefore, our data support isospin invariance in the region of the η-production threshold. Our transversity-up cross sections in forward direction closely follow the upper bound of the triangle inequalities; at very backward angles, both the transversity-up and -down CEX cross sections lie near the lower limit of the triangle inequalities.

ACKNOWLEDGMENTS

We thank J. E. Simmons and the LANL P-Division for the loan of the PPT and J. G. J. Boissevain and J. A. Holt for helping to set it up. W.J.B. wishes to acknowledge the support of the George Washington University Committee on Research and the NSF; while M.E.S. acknowledges the support of the Research Council at Abilene Christian University. This work was supported in part by the U.S. Department of Energy.

*Deceased.
†Present address: Physics Department, George Washington University, Washington, D.C. 20052.

[1]M. E. Sadler, W. J. Briscoe, D. H. Fitzgerald, B. M. K. Nefkens, and C. J. Seftor, Phys. Rev. D **35**, 2718 (1987).
[2]A. Mokhtari, A. D. Eichon, G. J. Kim, B. M. K. Nefkens, J. A. Wightman, D. H. Fitzgerald, W. J. Briscoe, and M. E. Sadler, Phys. Rev. D **35**, 810 (1987).
[3]W. S. C. Williams, *An Introduction to Elementary Particles* (Academic, New York, 1971).
[4]V. V. Abaev, V. S. Bekrenev, Yu. A. Beloglazov, V. G. Gaditsky, A. I. Kovalev, S. P. Kruglov, A. A. Kulbardis, I. V. Lopatin, A. N. Prokofiev, V. V. Sumachev, V. Yu. Trautman, E. P. Federova-Koval, E. A. Filimonov, and A. V. Shvedchikov, Z. Phys. A **311**, 217 (1983).
[5]R. M. Brown, A. G. Clark, J. K. Davies, J. DePagter, W. M. Evans, R. J. Gray, E. S. Groves, R. J. Ott, T. P. Shah, A. J. Shave, J. J. Thresher, and M. W. Tyrrell, Nucl. Phys. **B144**, 287 (1978).
[6]J. C. Alder, C. Joseph, J. P. Perroud, M. T. Tran, G. H. Eaton, R. Frosch, H. Hirschmann, S. Mango, J. W. McCulloch, P. Shrager, G. Strassner, P. Truöl, P. Weymouth, and P.

Wiederkehr, Phys. Rev. D **27**, 1040 (1983).
[7]J. C. Comiso, D. J. Blasberg, R. P. Haddock, B. M. K. Nefkens, P. Truöl, and L. J. Verhey, Phys. Rev. D **12**, 738 (1975).
[8]E. M. Henley and G. A. Miller, in *Mesons in Nuclei,* edited by M. Rho and D. Wilkinson (North-Holland, Amsterdam, 1979), pp. 405–434.
[9]R. E. Cutkosky, Phys. Lett. **88B**, 339 (1979).
[10]R. A. Arndt, L. D. Roper, and J. Ford, Phys. Rev. D **32**, 1085 (1985).
[11]G. Höhler, F. Kaiser, R. Koch, and E. Pietarinen, *Handbook of Pion-Nucleon Scattering* (Physics Data No. 12-1) (Fachinformationzentrum, Karlsruhe, 1978); R. Koch and E. Pietarinen, Nucl. Phys. **A336**, 331 (1980).
[12]R. E. Cutkosky, C. P. Forsyth, R. E. Hendrick, and R. L. Kelly, Phys. Rev. D **20**, 2839 (1979).
[13]R. Ayed and P. Bareyre, Paper No. 311 presented at the 11th International Conference on Elementary Particles, Aix-en-Provence, 1973 (unpublished).
[14]F. O. Borcherding, Ph.D. thesis, UCLA, 1982.
[15]D. Roeder and R. J. Macek, Los Alamos National Laboratory Report No. LA-7268-PR, 1977, pp. 31 and 32.
[16]W. J. Briscoe, D. H. Fitzgerald, B. M. K. Nefkens, and M. E. Sadler, Nucl. Instrum. Methods **197**, 277 (1982).
[17]J. A. Wightman, Ph.D. thesis, UCLA, 1987; J. A. Wightman, A. D. Eichon, G. J. Kim, A. Mokhtari, B. M. K. Nefkens, W. J. Briscoe, D. H. Fitzgerald, and M. E. Sadler, Phys. Rev. D **36**, 3529 (1987).
[18]W. B. Tippens, Ph.D. thesis, Texas A&M University, 1983; Los Alamos National Laboratory Report No. LA-9909-T, 1983 (unpublished); W. B. Tippens, T. S. Bhatia, G. Glass, J. C. Hiebert, R. A. Kenefick, L. C. Northcliffe, J. G. J. Boissevain, J. J. Jarmer, J. E. Simmons, D. H. Fitzgerald, J. Holt, A. Mokhtari, and G. E. Tripard, Phys. Rev. C **36**, 1413 (1987).
[19]G. J. Kim, Ph.D. thesis, UCLA, 1988.
[20]D. Menze, W. Pfeil, and R. Wilcke, *Compilation of Pion Photoproduction Data* (Physics Data No. 7-1) (ZAED, Bonn, 1977).